scientific reports

Check for updates

OPEN

Microstructure and hydrogen storage properties of the $Mg_{2-x}Y_xNi_{0.9}Co_{0.1}$ (x = 0, 0.2, 0.3, and 0.4) alloys

Defa Li[1], Feng Huang[2]✉, Bingzhi Ren[3], Shujie Wang[4], Wei Zhang[1] & Liming Zhu[2]

Rare earth elements have excellent catalytic effects on improving hydrogen storage properties of the Mg_2Ni-based alloys. This study used a small amount of Y to substitute Mg partially in $Mg_2Ni_{0.9}Co_{0.1}$ and characterized and discussed the effects of Y on the solidification and de-/hydrogenation behaviors. The $Mg_{2-x}Y_xNi_{0.9}Co_{0.1}$ (x = 0, 0.2, 0.3, and 0.4) hydrogen storage alloys were prepared using a metallurgy method. The phase composition of the alloys was studied using X-ray diffraction (XRD). Additionally, their microstructure and chemical composition were studied using scanning electron microscopy and energy-dispersive X-ray spectroscopy, respectively. The hydrogen absorption and desorption properties of the alloys were studied using pressure-composition isotherms and differential scanning calorimetric (DSC) measurements. The structure of the as-cast $Mg_2Ni_{0.9}Co_{0.1}$ alloy was composed of the peritectic Mg_2Ni, eutectic Mg–Mg_2Ni, and a small amount of pre-precipitated Mg–Ni–Co ternary phases, and was converted into the Mg_2NiH_4, $Mg_2Ni_{0.9}Co_{0.1}H_4$, and MgH_2 phases after hydrogen absorption. Furthermore, the XRD patterns of the alloys showed the $MgYNi_4$ phase and a trace amount of the Y_2O_3 phase along with the Mg and Mg_2Ni phases after the addition of Y. After hydrogen absorption, the phase of the alloys was composed of the Mg_2NiH_4, MgH_2, $MgYNi_4$, YH_3, Y_2O_3, and $Mg_2NiH_{0.3}$ phases. With the increase of Y addition, the area ratios of the peritectic Mg_2Ni matrix phase in the $Mg_{2-x}Y_xNi_{0.9}Co_{0.1}$ (x = 0, 0.2, 0.3, and 0.4) alloys gradually decreased until they disappeared. However, the eutectic structure gradually increased, and the microstructures of the alloys were obviously refined. The addition of Y improves the activation performance of the alloys. The alloy only needed one cycle of de-/hydrogenation to complete the activation for x = 0.4. The DSC curves showed that the initial dehydrogenation temperatures of $Mg_2Ni_{0.9}Co_{0.1}$ and $Mg_{1.8}Y_{0.2}Ni_{0.9}Co_{0.1}$ were 200 and 156 °C, respectively. The desorption activation energies of the hydrides of the $Mg_2Ni_{0.9}Co_{0.1}$ and $Mg_{1.8}Y_{0.2}Ni_{0.9}Co_{0.1}$ alloys calculated using the Kissinger method were 94.7 and 56.5 kJ/mol, respectively. Moreover, the addition of Y reduced the initial desorption temperature of the alloys and improved their kinetic properties.

Hydrogen energy has been widely studied and is considered a green energy expected to replace petroleum because of its advantages, such as clean energy, abundant reserves, and good combustion performance[1–3]. The current research on hydrogen is mainly focused on its production, storage, transportation, and application. Although the preparation and application technology of hydrogen is relatively mature, hydrogen storage is a major problem that needs to be solved. Hydrogen storage technology is the key to widely applying hydrogen as a fuel[4].

A_2B type magnesium series hydrogen storage alloy, Mg_2Ni, is regarded as one of the most promising hydrogen storage materials in the twenty-first century since it has a high hydrogen storage capacity, low price, and abundant resources. However, its disadvantages, such as slow kinetics, over-stable hydride, and high hydrogen desorbing temperature, hinder its use in practical applications[5–7]. Consequently, extensive research, including alloying[8–10], doping of catalysts[11,12], and fabrication of composites[13–15], has been done to overcome this obstacle and enable

[1]School of Mechanical and Vehicle Engineering, West Anhui University, Luan 237012, China. [2]Hubei Key Laboratory of Advanced Technology for Automotive Components, Wuhan University of Technology, Wuhan 430070, China. [3]School of Metallurgy and Materials Engineering, Chongqing University of Science and Technology, Chongqing 401331, China. [4]The 13th Research Institute, CETC, Shijiazhuang 050051, China. ✉email: 303_Lee@163.com

it to meet the requirements of the U.S. Department of Energy for hydrogen storage materials. Many methods showed significant improvement in the hydrogen storage performance of the Mg_2Ni type alloys by substituting Ni or Mg with transition or rare earth elements, respectively, especially its thermodynamic properties could be adjusted to enable it to meet the requirements of practical applications[16]. Song et al. believed that partially substituting Mg with Nd could improve the activation property of the Mg_2Ni alloy[17]. Consequently, it was reported for the first time that the hydrogen absorption capacity of $Mg_{1.9}Nd_{0.1}Ni$ reached 2.86 wt%, which was higher than that of Mg_2Ni since the multiphase structure formed by substituting Mg with Nd increased the phase boundary area and provided a favorable path for the diffusion of hydrogen atoms. Kalinichenka et al. showed that the Mg–Ni–Y system is highly suitable for reversible hydrogen storage[18]. The $Mg_{80}Ni_{10}Y_{10}$ and $Mg_{90}Ni_5Y_5$ alloys have a high hydrogen absorption rate under the hydrogen pressure of 20 bar, even at 250 °C. According to Li et al. and Zhang et al., the addition of Y improved the hydrogen absorption and desorption thermodynamics of the MgNi-based alloys[19,20]. Xie et al. used the hydrogen plasma metal reaction (HPMR) method to successfully prepare $Mg_2Ni_{1-x}Co_x$ (x = 0, 0.05, and 0.1) alloys and found that adding Co improved their hydrogen absorption kinetic properties significantly[21].

Therefore, the literature review shows that the partial substitution of the A and B-side elements with Y and Co, respectively, contribute to improving the hydrogen storage performance of the Mg_2Ni alloy[22–25]. However, few reports exist on the simultaneous addition of Y and Co. Thus, this study used the rare earth element Y and the transition element Co to replace Mg partially and Ni on the basis of Mg_2Ni alloy, respectively, to realize the dual regulation of de-/hydrogenation kinetics and thermodynamic properties of the Mg_2Ni alloy.

Experimental procedure

Preparation of the $Mg_{2-x}Y_xNi_{0.9}Co_{0.1}$ samples

Commercially pure Mg (99.9% purity), Mg–Ni intermediate alloy (70 wt% Ni content, 99.9% purity), Mg–Y intermediate alloy (30 wt% Y content, 99.9% purity), and pure Co (99.9% purity) were used as raw materials to prepare $Mg_{2-x}Y_xNi_{0.9}Co_{0.1}$ (x = 0, 0.2, 0.3, and 0.4) alloy ingots in a graphite crucible in an electric resistance furnace, under the protection of a mixed flow of SF_6 and CO_2. Intermittent mechanical agitation was conducted during smelting to prevent density segregation of the alloy melt. Moreover, additional Mg (2 wt%) was added to compensate for its inherent evaporation loss. Subsequently, the desired ingot could be obtained as the melt was cooled to room temperature in a furnace. The weight of each ingot was approximately 80 g.

Furthermore, the de-/hydrogenation measurement samples were taken from the center of each ingot. Prior to tests, the samples were mechanically broken, followed by ball-milling in a high-energy ball mill (HEBM) at a rotating speed of 240 rpm for about 60 min. The ball-to-material ratio during ball milling was 30:1, and high-purity argon (99.999% purity) was inserted to prevent oxidation. Additionally, intermittent ball milling was adopted to avoid the adhesion of components and excessively high temperature caused by long-duration ball milling. In intermittent ball milling, the rotation is stopped after 20 min for 15 min, then reversed until 60 min of ball milling is completed. Subsequently, about 0.5 g of 200-mesh powder was screened for the hydrogen storage performance test.

Characterization and de-/hydrogenation measurements

The phases in the as-cast ingots and hydrogenated powders were identified using X-ray diffraction (XRD) with Cu Kα radiation for continuous scanning at a rate of 2°/min in the 2θ range of 10–85°. The microstructures were characterized using scanning electron microscopy (SEM), and the corresponding chemical compositions were analyzed using energy-dispersive X-ray spectroscopy (EDS). Meanwhile, Image-Pro Plus (IPP) was used for counting the phase area ratios in the SEM images.

After activation, the isothermal de-/hydrogenation performance of the ball-milled alloys was measured using a precise volumetric Sieverts-type apparatus at 260, 280, and 300 °C, with hydrogen pressure of 2.5 and 0.1 MPa for hydrogen absorption and desorption, respectively. The differential scanning calorimetric (DSC) measurements were conducted from room temperature to 450 °C at the heating rates of 5, 10, and 15 °C/min under 50 mL/min argon gas flow to characterize the phase transformation behaviors of the hydrides.

Results and discussion

Phase compositions of the as-cast alloys

The XRD patterns of the as-cast $Mg_{2-x}Y_xNi_{0.9}Co_{0.1}$ (x = 0, 0.2, 0.3, and 0.4) alloys are shown in Fig. 1. The diffraction peaks of the tested alloys were pointy, indicating their crystallization characteristics. $Mg_2Ni_{0.9}Co_{0.1}$ was only composed of the Mg and Mg_2Ni phases. As shown in the Mg–Ni binary alloy diagram in Fig. 2, the solidification path of Mg_2Ni under equilibrium solidification conditions should be: $L \rightarrow L + MgNi_2 \rightarrow L + Mg_2Ni \rightarrow Mg + Mg_2Ni$. The absence of the $MgNi_2$ peaks in the $Mg_2Ni_{0.9}Co_{0.1}$ diffraction profile indicated that all the primary $MgNi_2$ was transformed into Mg_2Ni though a peritectic reaction with liquid at 760 °C or the residual $MgNi_2$ was rare and diffused. Thus, the alloy was near-equilibrium solidified during furnace cooling in this study.

$MgYNi_4$ and Y_2O_3 diffraction peaks were obviously present in the XRD patterns of $Mg_{2-x}Y_xNi_{0.9}Co_{0.1}$ (x = 0.2, 0.3, and 0.4) along with Mg and Mg_2Ni diffraction peaks when Y was added to substitute Mg partially. $MgYNi_4$ belonged to Laves phase and had a C15 structure, which agreed well with Reference[26]. According to Reference[26], the added Y was first dissolved in primary $MgNi_2$ to replace Mg, and then $MgNi_2$ reached the composition and transformed into $MgYNi_4$ when the Y content increased, and the Mg content decreased in $MgNi_2$. Meanwhile, it can be inferred from the high diffraction intensity shown in Fig. 1 that the converted $MgYNi_4$ was largely absent from the subsequent peritectic reaction and was retained in the $Mg_{2-x}Y_xNi_{0.9}Co_{0.1}$ alloy.

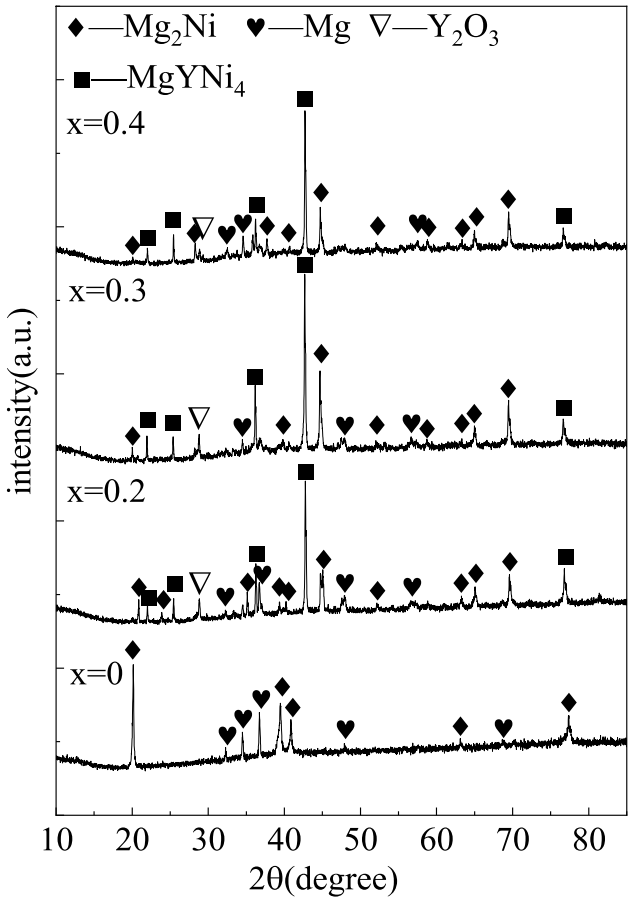

Figure 1. XRD patterns of the as-cast $Mg_{2-x}Y_xNi_{0.9}Co_{0.1}$ (x = 0, 0.2, 0.3, and 0.4) alloys.

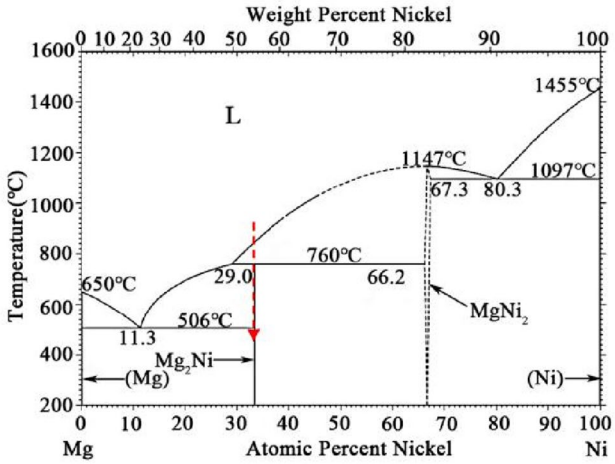

Figure 2. The Mg–Ni binary alloy phase diagram.

Microstructures of the as-cast alloys

The scanning electron microscope equipped with backscattered electrons detector (SEM/BSE) images of the as-cast $Mg_{2-x}Y_xNi_{0.9}Co_{0.1}$ (x = 0, 0.2, 0.3, and 0.4) alloys are shown in Fig. 3, and the corresponding EDS results are listed in Table 1. Based on the SEM images, EDS results, and the solidification path discussed, the as-cast $Mg_2Ni_{0.9}Co_{0.1}$ was composed of gray block peritectic Mg_2Ni and dark lamellar eutectic Mg–Mg_2Ni, with some bright fine primary $MgNi(Co)_2$ dispersed in the matrix, as shown in Fig. 3a and b. Meanwhile, the remaining

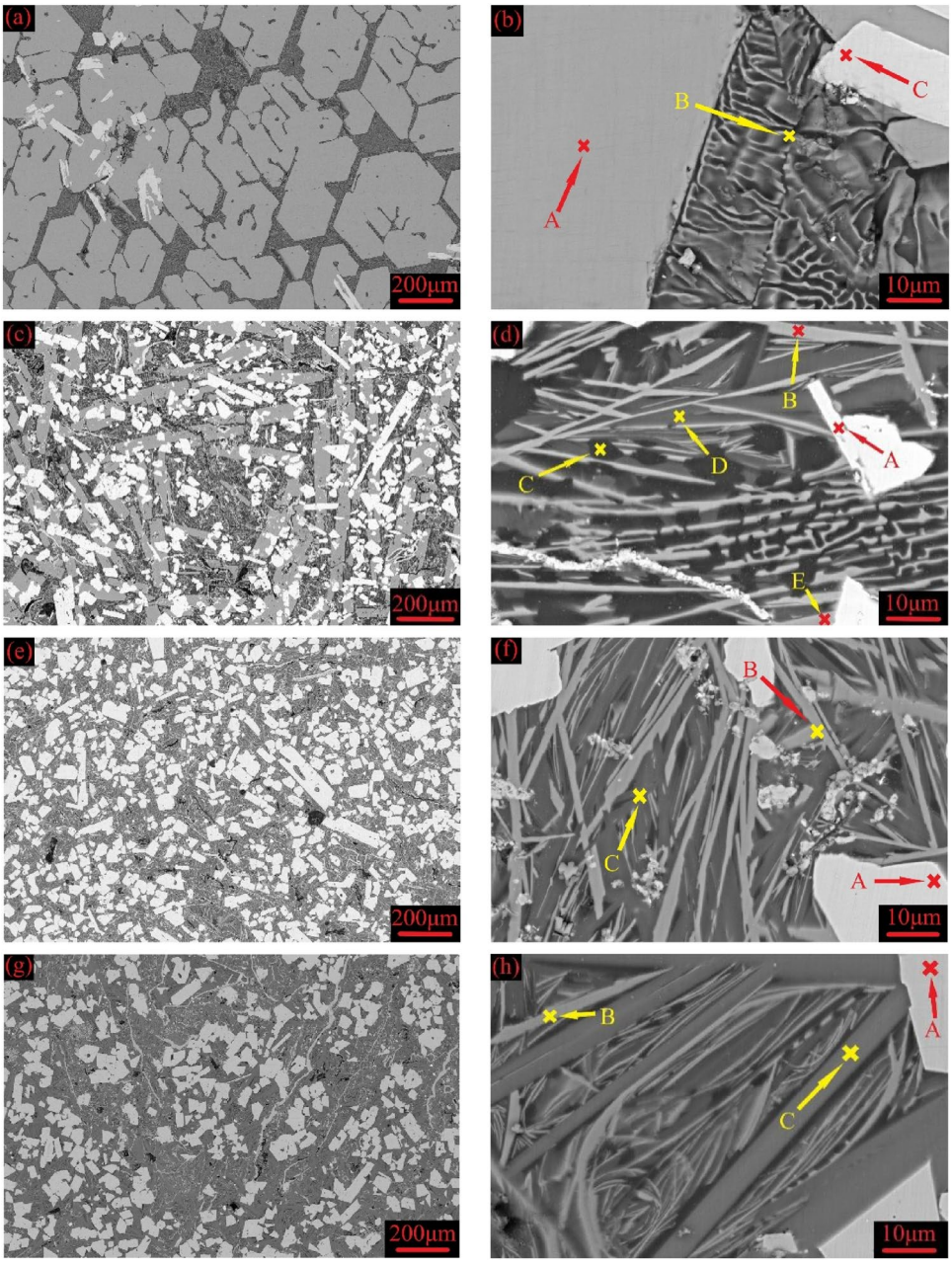

Figure 3. SEM/BSE images of the as-cast $Mg_{2-x}Y_xNi_{0.9}Co_{0.1}$ alloys at low and high magnification for (**a** and **b**) x = 0, (**c** and **d**) x = 0.2, (**e** and **f**) x = 0.3, and (**g** and **h**) x = 0.4.

primary $MgNi(Co)_2$ was not found in the XRD test due to its small quantity and fine dispersion distribution characteristics.

As shown in Fig. 3c,e, and g, $Mg_{2-x}Y_xNi_{0.9}Co_{0.1}$(x = 0.2, 0.3, and 0.4) alloys had largely increased amounts of the bright phase compared with $Mg_2Ni_{0.9}Co_{0.1}$. Additionally, the corresponding EDS results showed that they were primary $MgYNi_4$, coinciding well with the XRD results. Meanwhile, the original peritectic Mg_2Ni block was refined and elongated after a small Y content (x = 0.2) was added, as shown in Fig. 3c. Furthermore, the primary precipitation phase was all $MgYNi_4$, and the subsequent peritectic reaction was inhibited when the Y content increased above 0.3, resulting in the disappearance of peritectic Mg_2Ni. Consequently, the $Mg_{1.7}Y_{0.3}Ni_{0.9}Co_{0.1}$ and $Mg_{1.6}Y_{0.4}Ni_{0.9}Co_{0.1}$ alloys were only composed of bright primary $MgYNi_4$ and dark lamellar eutectic Mg-Mg_2Ni.

Unlike the $Mg_2Ni_{0.9}Co_{0.1}$ alloy, the $Mg_{1.8}Y_{0.2}Ni_{0.9}Co_{0.1}$ alloy had four regions with contrasting degrees. The results obtained using EDS analysis of the composition of each region are shown in Table 1. Combined with the XRD results of the alloys, it could be seen that the bright white region A embedded in the matrix was the first precipitation of the $MgYNi_4$ phase. The elongated acicular gray region B was the eutectic Mg_2Ni phase, the black region C around the acicular Mg_2Ni phase was the eutectic α-Mg phase (Mg phase without a solid solution of other elements), and the gray-black region D was the eutectic ε-Mg phase (Mg phase with small amounts of Ni

Alloy	Position	Weight%				Atomic%				Phase
		Mg	Y	Ni	Co	Mg	Y	Ni	Co	
$Mg_2Ni_{0.9}Co_{0.1}$	A	48.06	–	50.3	1.91	69.09	–	29.78	1.13	Mg_2Ni
	B	69.4	–	29.4	1.11	84.5	–	14.8	0.5	$Mg+Mg_2Ni$
	C	20.8	–	68.2	10.8	38.9	–	52.7	8.3	$MgNi(Co)_2$
$Mg_{1.8}Y_{0.2}Ni_{0.9}Co_{0.1}$	A	8.19	24.6	67.1	–	19.1	15.7	65.0	–	$MgYNi_4$
	B	47.5	6.42	45.9	–	69.5	2.57	27.8	–	Mg_2Ni
	C	100	0	0	–	100	0	0	–	α-Mg
	D	79.5	11.8	8.56	–	92.1	3.76	4.11	–	ε-Mg
	E	44.1	4.44	51.4	–	66.2	1.82	31.9	–	Mg_2Ni
$Mg_{1.7}Y_{0.3}Ni_{0.9}Co_{0.1}$	A	8.0	25.6	66.3	–	18.8	16.5	64.6	–	$MgYNi_4$
	B	47.7	7.22	45.0	–	69.8	2.89	27.2	–	Mg_2Ni
	C	75.1	14.0	10.7	–	90.0	4.6	5.35	–	ε-Mg
$Mg_{1.6}Y_{0.4}Ni_{0.9}Co_{0.1}$	A	8.68	27.0	64.2	–	20.3	17.3	62.3	–	$MgYNi_4$
	B	46.3	9.42	44.2	–	68.9	3.83	27.2	–	Mg_2Ni
	C	68.4	20.2	11.2	–	87.0	7.04	5.94	–	ε-Mg

Table 1. EDS results of the as-cast $Mg_{2-x}Y_xNi_{0.9}Co_{0.1}$ (x = 0, 0.2, 0.3, and 0.4) alloys.

and Y elements). The elongated gray region E was the matrix phase of peritectic Mg_2Ni. As seen in Fig. 3c, the region composed of B, C, and D was located in the gap of the peritectic Mg_2Ni matrix phase, and it should be the eutectic structure composed of Mg and Mg_2Ni. Compared with the $Mg_2Ni_{0.9}Co_{0.1}$ alloy, the eutectic structure of the $Mg_{1.8}Y_{0.2}Ni_{0.9}Co_{0.1}$ alloy was finer and not lamellar. Simultaneously, the peritectic Mg_2Ni phase changed from a thick block to a long strip, indicating that the addition of Y benefitted in refining the microstructure of the alloy.

Compared with the $Mg_{1.8}Y_{0.2}Ni_{0.9}Co_{0.1}$ alloy, the peritectic Mg_2Ni and eutectic α-Mg phases disappeared in the $Mg_{1.7}Y_{0.3}Ni_{0.9}Co_{0.1}$ alloy. In other words, the first precipitated $MgNi_2$ phase of the alloy was converted into $MgYNi_4$ under the condition of non-equilibrium solidification when the added Y content increased to 0.3, but $MgYNi_4$ did not participate in the peritectic reaction, leading to the precipitation of no peritectic Mg_2Ni phase in the alloy. With the further decrease in temperature, the eutectic reaction occurred in the remaining alloy melt, forming the eutectic structure. Due to the high Y content in the melt, Y was dissolved in α-Mg in the eutectic structure to convert it to ε-Mg. Furthermore, the EDS analysis showed that the phase composition of the alloy did not change when the added Y content was increased to 0.4. $Mg_{1.6}Y_{0.4}Ni_{0.9}Co_{0.1}$ and $Mg_{1.7}Y_{0.3}Ni_{0.9}Co_{0.1}$ had the same solidification path, where $MgYNi_4$ was precipitated first, followed by the precipitation of Mg_2Ni and ε-Mg through eutectic reactions.

The phase area ratios in the SEM images were counted using IPP to describe the effect of Y addition on the microstructure of the alloy more intuitively, and the corresponding statistically calculated results are shown in Fig. 4. Clearly, the peritectic reaction was inhibited when the added Y content was above 0.2. Compared with $Mg_2Ni_{0.9}Co_{0.1}$, the area ratio of the peritectic Mg_2Ni decreased from 67 to 21% when a small amount of Y (x = 0.2) was added. Meanwhile, more melt was retained at low temperatures to conduct the eutectic reaction since the peritectic reaction was inhibited, increasing the area ratio of eutectic Mg–Mg_2Ni with increased Y content. The maximum area ratio for $MgYNi_4$ was obtained when the added Y content was 0.3. Thus, the added Y was first dissolved in primary $MgNi_2$, which was converted into $MgYNi_4$ when Y reached the corresponding content in the $Mg_{2-x}Y_xNi_{0.9}Co_{0.1}$ alloy. The solidification path was $L \rightarrow L + Mg(Y)Ni_2 \rightarrow L + MgYNi_4 + Mg(Y)Ni_2 \rightarrow L + MgYNi_4 + Mg_2Ni(peritectic) \rightarrow MgYNi_4 + Mg_2Ni(peritectic) + Mg–Mg_2Ni(eutectic)$. Notably, all $Mg(Y)Ni_2$ would be

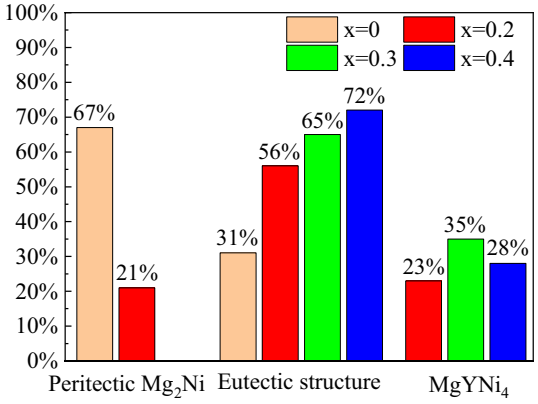

Figure 4. Phase area ratios in $Mg_{2-x}Y_xNi_{0.9}Co_{0.1}$ (x = 0, 0.2, 0.3, and 0.4) alloys.

converted into MgYNi4 when the added Y content was above 0.2, inhibiting the peritectic reaction and disappearance of peritectic Mg_2Ni in the final solidified structures. Thus, the $MgYNi_4$ amount in the final solidified microstructure depended on the amounts of primary Mg(Y)Ni2 and Y that could participate in the reaction during solidification. The amount of the primary $Mg(Y)Ni_2$ decreased when the added Y content was further increased from 0.3 to 0.4, reducing the final transformed $MgYNi_4$, as shown in Fig. 4. The excess Y will dissolved into Mg–Mg_2Ni eutectic during subsequent solidification, resulting in the higher Y content dissolved in eutectic Mg-Mg_2Ni in $Mg_{1.6}Y_{0.4}Ni_{0.9}Co_{0.1}$ than that in $Mg_{1.7}Y_{0.3}Ni_{0.9}Co_{0.1}$ and $Mg_{1.8}Y_{0.2}Ni_{0.9}Co_{0.1}$, as shown in Table 1. In addition to the phase composition discussed, adding Y significantly refined the solidification structure, as seen in Fig. 3.

Activation and de-/hydrogenation properties

Since an impurity layer composed of oxides and hydroxides is usually formed on the surface of ball-milled alloy particles, activation is necessary to break this surface impurity layer and expose the fresh alloy metal inside. This study carried out the activation through three successive de-/hydrogenation circles at 300 °C. Hydrogenation and dehydrogenation were conducted under 2.5 and 0.1 MPa hydrogen pressure, respectively. Meanwhile, this study tested and discussed only the activation and de-/hydrogenation properties of $Mg_{2-x}Y_xNi_{0.9}Co_{0.1}$ (x = 0, 0.2, and 0.4) since the peritectic reaction was inhibited and $Mg_{1.7}Y_{0.3}Ni_{0.9}Co_{0.1}$ exhibited microstructures similar to that of $Mg_{1.6}Y_{0.4}Ni_{0.9}Co_{0.1}$.

The activation hydrogen absorption curves of the $Mg_{2-x}Y_xNi_{0.9}Co_{0.1}$ (x = 0, 0.2, and 0.4) alloys are shown in Fig. 5. Comparing the time required to reach the maximum hydrogen absorption capacity for the first hydrogen absorption curve, the hydrogen absorption rate of the three alloys in descending order was: $Mg_{1.6}Y_{0.4}Ni_{0.9}Co_{0.1}$, $Mg_{1.8}Y_{0.4}Ni_{0.9}Co_{0.1}$, and $Mg_2Ni_{0.9}Co_{0.1}$. Unlike the hydrogen absorption rate, the maximum hydrogen absorption capacity in descending order was: $Mg_2Ni_{0.9}Co_{0.1}$ (3.13 wt%), $Mg_{1.8}Y_{0.4}Ni_{0.9}Co_{0.1}$ (2.17 wt%), and $Mg_{1.6}Y_{0.4}Ni_{0.9}Co_{0.1}$ (1.79 wt%). Therefore, the addition of Y improved the hydrogen absorption rate but decreased the hydrogenation capacity. Additionally, the third hydrogen absorption curve coincided with the second hydrogen absorption curve, indicating that the three alloys could be completely activated after two successive de-/hydrogenation circles.

Unlike $Mg_2Ni_{0.9}Co_{0.1}$, $Mg_{1.8}Y_{0.2}Ni_{0.9}Co_{0.1}$ and $Mg_{1.6}Y_{0.4}Ni_{0.9}Co_{0.1}$ had slightly lower hydrogen absorption capacities after activation than before activation due to the formation of YH_3. When Y is added, YH_3 is formed during hydrogen absorption, followed by conversion to YH_2 during dehydrogenation. The dehydrogenation

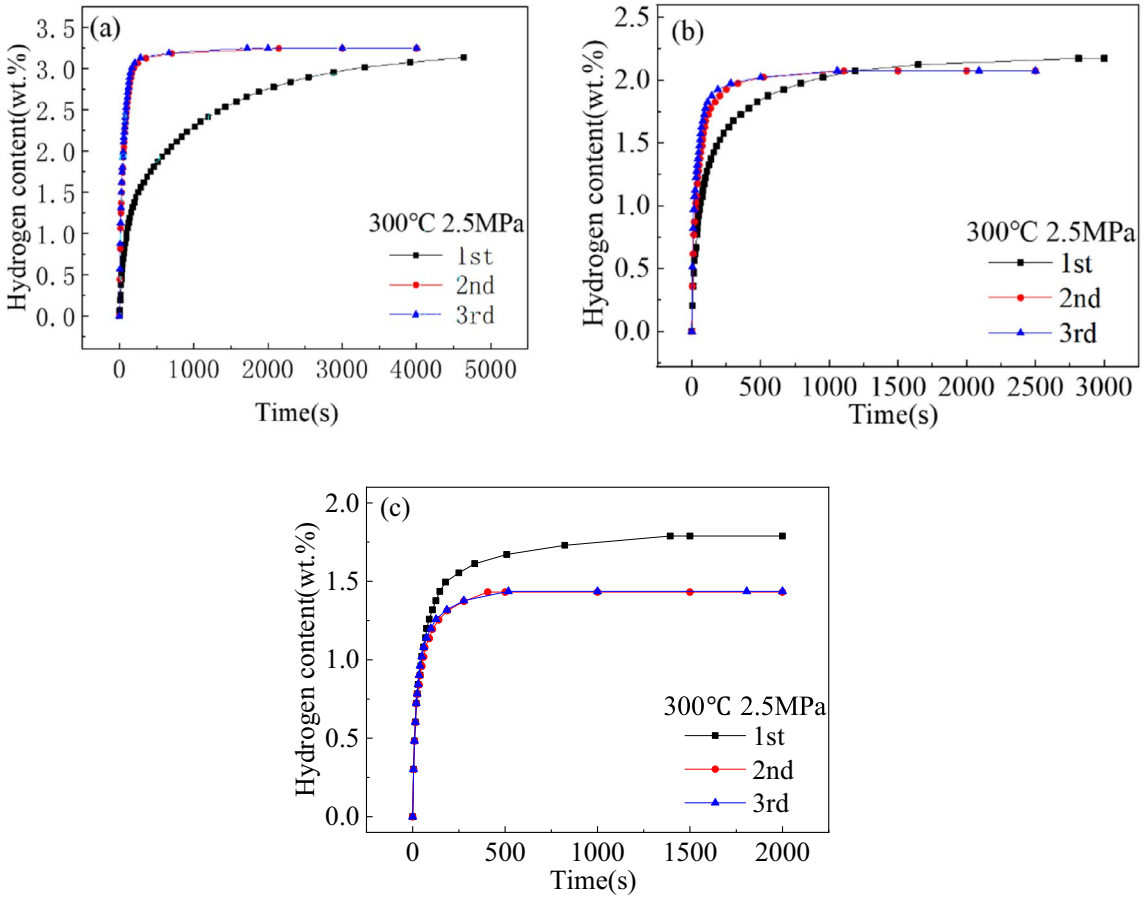

Figure 5. Activation hydrogen absorption curves of $Mg_{2-x}Y_xNi_{0.9}Co_{0.1}$ alloys for (**a**) x = 0, (**b**) x = 0.2, and (**c**) x = 0.4.

temperature of YH_2 is about 1063 K[27], which is obviously much higher than the activation temperature in this study. Consequently, YH_2 could not be dehydrogenated and was left, resulting in the decreased hydrogen absorption capacity of the alloy in the subsequent hydrogen absorption process. Meanwhile, $Mg_{1.6}Y_{0.4}Ni_{0.9}Co_{0.1}$ had a more obvious reduction in the hydrogen absorption capacity after activation since $Mg_{1.6}Y_{0.4}Ni_{0.9}Co_{0.1}$ had a larger Y content than $Mg_{1.8}Y_{0.2}Ni_{0.9}Co_{0.1}$, as shown in Fig. 5b and c.

Due to its low average atomic density and the large space between atoms, hydrogen diffused more easily through the phase boundary[28]. As discussed in Section "Microstructures of the as-cast alloys", the area ratio of eutectic structures increased, and the solidification structure was refined with the increased Y content, improving the activation property of the alloys.

The hydrogen absorption capacity and rate at different temperatures are important indexes to reflect the hydrogen absorption kinetics of the alloys. The hydrogen absorption kinetic curves of $Mg_{2-x}Y_xNi_{0.9}Co_{0.1}$ (x = 0, 0.2, and 0.4) alloys at different temperatures are shown in Fig. 6. All the three alloys showed a fast hydrogen absorption rate after being fully activated, reaching more than 80% of the corresponding maximum hydrogen absorption capacity in only 6 min. As shown in Section "Microstructures of the as-cast alloys", $MgYNi_4$ was formed when Y was added, and its proportion increased with the increased Y content. The maximum hydrogen absorption capacity of $Mg_{2-x}Y_xNi_{0.9}Co_{0.1}$ (x = 0, 0.2, and 0.4) decreased with the increased Y content, from 3.31 wt% to 1.99 wt% and then to 1.67 wt% at 260 °C due to the presence of the non-hydrogen absorbing phase.

The maximum hydrogen absorption capacity of the $Mg_2Ni_{0.9}Co_{0.1}$ alloy was 3.13 wt% at 2.5 MPa hydrogen pressure and 300 °C temperature, and the time taken to reach the maximum hydrogen absorption capacity was 22 min. Under the same reaction conditions, $Mg_{2-x}Y_xNi_{0.9}Co_{0.1}$ (x = 0.2 and 0.4) alloys could reach more than 90% of the maximum hydrogen absorption capacity in 200 s. By comparison, the maximum hydrogen absorption of the alloys decreased with the addition of Y due to the formation of the $MgYNi_4$ phase that does not absorb hydrogen and the unsaturated hydride $Mg_2NiH_{0.3}$ in the $Mg_{2-x}Y_xNi_{0.9}Co_{0.1}$ (x = 0.2 and 0.4) alloys during the hydrogen absorption process.

The hydrogen desorption kinetic curves of $Mg_{2-x}Y_xNi_{0.9}Co_{0.1}$ (x = 0, 0.2, and 0.4) alloys at 0.1 MPa hydrogen pressure after hydrogen absorption under the conditions mentioned are shown in Fig. 7. The comparison of the de-/hydrogenation kinetic curves of the alloys showed that the complete hydrogen desorption of alloys required significantly lower time than the hydrogen absorption process. The hydride layer on the surface of the alloys hinders the diffusion of hydrogen atoms into the alloys during their hydrogen absorption process. However, this hydride layer on the surface of the alloys breaks down during the desorption process to produce hydrogen atoms that do not need to pass through the hydride layer but only through the metal surface. Since the diffusion rate

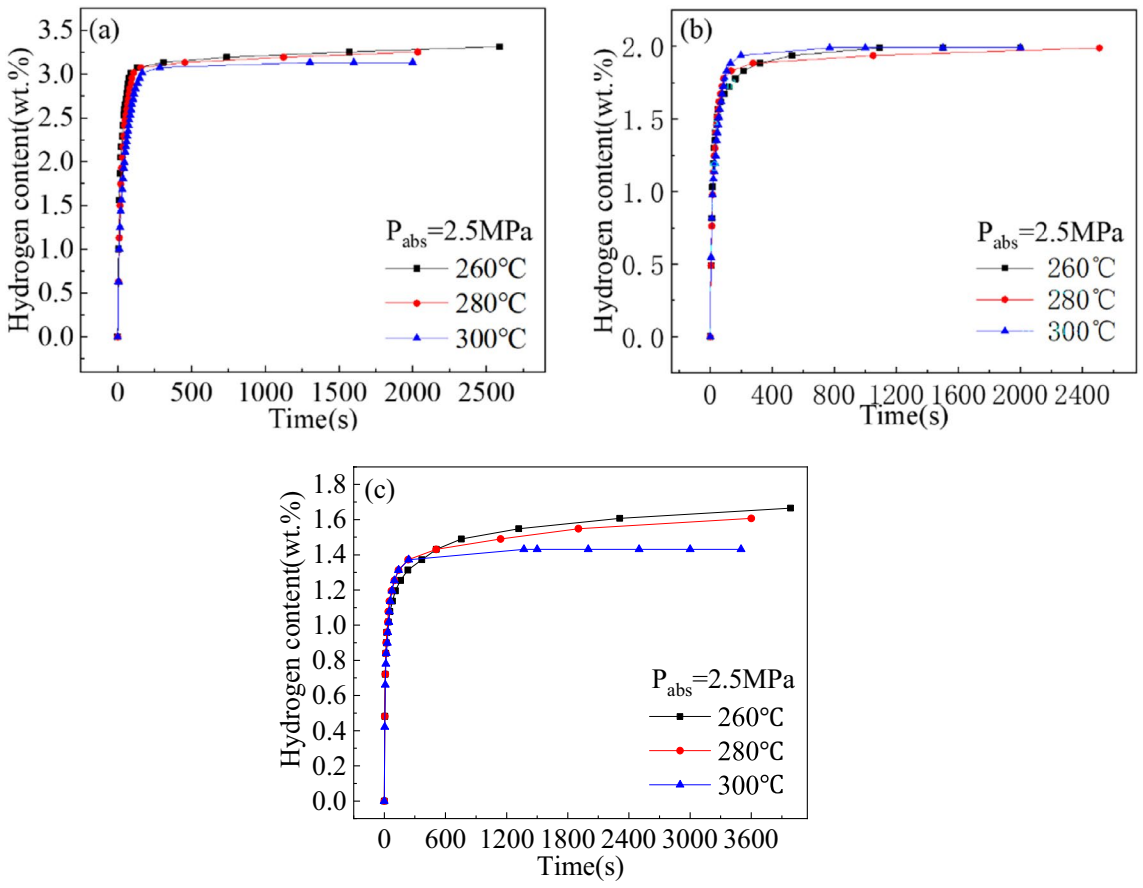

Figure 6. Hydrogen absorption kinetic curves of $Mg_{2-x}Y_xNi_{0.9}Co_{0.1}$ alloys at different temperatures for (**a**) x = 0, (**b**) x = 0.2, and (**c**) x = 0.4.

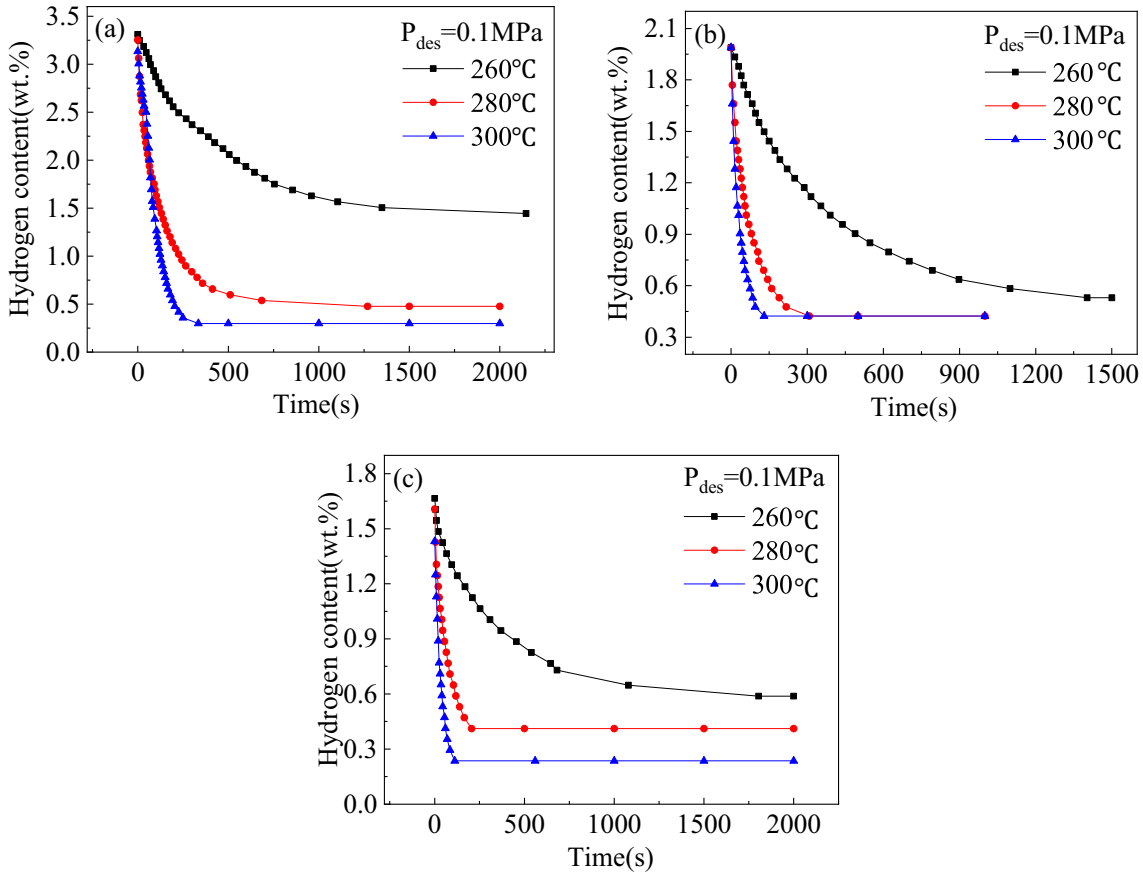

Figure 7. Hydrogen desorption kinetic curves of the $Mg_{2-x}Y_xNi_{0.9}Co_{0.1}$ alloys at different temperatures for (**a**) x = 0, (**b**) x = 0.2, and (**c**) x = 0.4.

of the hydrogen atoms in the hydride was much lower than that in the metal surface[29], the complete hydrogen desorption of the alloys required significantly lower time than the complete hydrogen absorption. Additionally, the maximum hydrogen discharges of the three alloys increased with the increase in temperature since the dehydrogenation of the alloy is a reversible process and the hydrogen absorption and desorption reactions occur simultaneously, where the absorption and desorption processes are exothermic and endothermic reactions, respectively. The hydrogen desorption of the alloys would increase with the increase in temperature since the temperature is conducive to the desorption process. The dehydrogenation capacities of the $Mg_{2-x}Y_xNi_{0.9}Co_{0.1}$ (x = 0, 0.2, and 0.4) alloys at different temperatures for 50 s are shown in Table 2. The dehydrogenation amounts of the alloys for x = 0, 0.2, and 0.4 were 0.19, 0.22, and 0.24 wt% after hydrogen desorption for 50 s at 260 °C, respectively, indicating that the addition of Y improved the desorption kinetic properties of the alloys. However, this phenomenon was not observed at higher reaction temperatures.

Hydrogen absorption reaction mechanism of alloys

The XRD patterns of the $Mg_{2-x}Y_xNi_{0.9}Co_{0.1}$ (x = 0, 0.2, and 0.4) alloy hydrides after hydrogen absorption at 300 °C and 2.5 MPa are shown in Fig. 8. The $Mg_2Ni_{0.9}Co_{0.1}$ alloy hydride was mainly composed of Mg_2NiH_4, MgH_2, and $Mg_2Ni_{0.9}Co_{0.1}H_4$. The Mg_2(Ni, Co) solid solution formed in Mg_2Ni by partial Co solution reacted with hydrogen to form $Mg_2Ni_{0.9}Co_{0.1}H_4$. According to Hayakawa et al. $Mg_2Ni_{0.9}Co_{0.1}H_4$ is another polymorph of Mg_2NiH_4, the distortion product of the cubic HT- Mg_2NiH_4[30].

Alloy	Dehydrogenation Capacity (wt%)		
	260 °C	280 °C	300 °C
x = 0	0.19	1.13	0.76
x = 0.2	0.22	0.87	1.25
x = 0.4	0.24	0.66	0.9

Table 2. Dehydrogenation capacities of the $Mg_{2-x}Y_xNi_{0.9}Co_{0.1}$ (x = 0, 0.2, and 0.4) alloys at different temperatures.

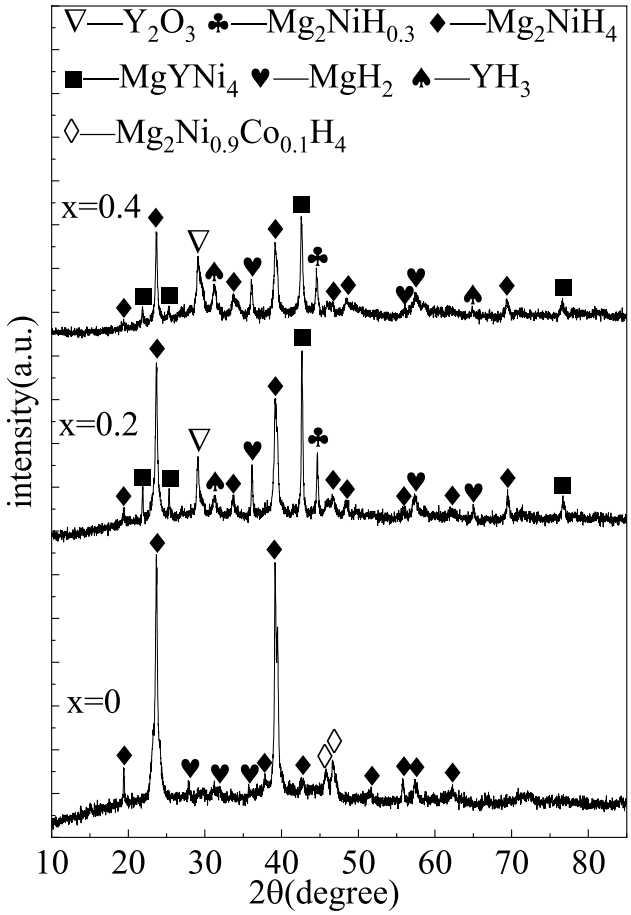

Figure 8. XRD patterns of the $Mg_{2-x}Y_xNi_{0.9}Co_{0.1}$ (x = 0, 0.2, 0.4) alloy hydrides.

Combined with the XRD patterns and EDS analysis, the hydrogen absorption reaction of the $Mg_2Ni_{0.9}Co_{0.1}$ alloy can be expressed as follows:

$$Mg + H_2 \rightarrow MgH_2 \quad (1)$$

$$Mg_2Ni + 2H_2 \rightarrow Mg_2NiH_4 \quad (2)$$

$$Mg_2(Ni,\ Co) + 2H_2 \rightarrow Mg_2Ni_{0.9}Co_{0.1}H_4 \quad (3)$$

Additionally, no other Co phases except the $Mg_2Ni_{0.9}Co_{0.1}H_4$ phase were found in the XRD pattern of the $Mg_2Ni_{0.9}Co_{0.1}$ alloy hydride. Therefore, it could be concluded that the Mg–Ni–Co phase did not undergo hydrogen absorption or decomposition reaction under the experimental conditions of this study, which is consistent with the fact that $MgNi_2$ in the Mg_2Ni alloy did not undergo the hydrogen absorption reaction[31].

The XRD patterns of the $Mg_{2-x}Y_xNi_{0.9}Co_{0.1}$ (x = 0.2 and 0.4) alloys after hydrogen absorption showed that both of them were composed of Mg_2NiH_4, MgH_2, $MgYNi_4$, YH_3, Y_2O_3, and $Mg_2NiH_{0.3}$. The $Mg_2NiH_{0.3}$ phase was an intermediate product in the hydrogen absorption reaction of Mg_2Ni to form Mg_2NiH_4, an unsaturated hydride. Since the samples were ball-milled in the argon atmosphere and the operation of taking out the samples and loading them into the reactor was performed in a glove box, the trace Y element in the alloy would not be completely oxidized, and YH_3 would be formed in the hydrogen absorption process. The intensity of the YH_3 diffraction peak increased slightly with the increased Y content, indicating that more Y was involved in the reaction to form YH_3 in the hydrogen absorption process of the alloys with the increased substitution of Y.

Combined with the XRD patterns and EDS analysis, the hydrogen absorption reaction of the $Mg_{2-x}Y_xNi_{0.9}Co_{0.1}$ (x = 0.2 and 0.4) alloys can be expressed as follows:

$$Mg + H_2 \rightarrow MgH_2 \quad (4)$$

$$Mg_2Ni + H_2 \rightarrow Mg_2NiH_{0.3} \quad (5)$$

$$Mg_2NiH_{0.3} + H_2 \rightarrow Mg_2NiH_4 \quad (6)$$

$$Y + H_2 \rightarrow YH_3 \quad (7)$$

Hydrogen release process of alloys hydride

The phase transition of the $Mg_{2-x}Y_xNi_{0.9}Co_{0.1}$ (x = 0, 0.2, and 0.4) alloy hydrides during dehydrogenation was studied using DSC measurements. The DSC curves of the $Mg_{2-x}Y_xNi_{0.9}Co_{0.1}$ (x = 0, 0.2, and 0.4) alloy hydrides at a heating rate of 5 °C/min are shown in Fig. 9. The DSC curve of the $Mg_2Ni_{0.9}Co_{0.1}$ alloy hydride had two endothermic peaks, with the smaller endothermic peak at 236 °C. The main endothermic peak had a peak temperature of 263.5 °C. The XRD pattern of the $Mg_2Ni_{0.9}Co_{0.1}$ alloy hydride showed that the hydrogen desorption phases included Mg_2NiH_4, MgH_2, and $Mg_2Ni_{0.9}Co_{0.1}H_4$. $Mg_2Ni_{0.9}Co_{0.1}H_4$ was a metastable phase produced by the reaction between the Mg_2(Ni, Co) solid solution and hydrogen. As reported in the literature, the peak desorption temperatures of Mg_2NiH_4 and MgH_2 were 247–287 °C and 327–387 °C, respectively[32]. It was inferred that the endothermic peak at 236 °C corresponded to the dehydrogenation process of the metastable $Mg_2Ni_{0.9}Co_{0.1}H_4$, and the main endothermic peak at 263.5 °C corresponded to the hydrogen desorption process of the Mg_2NiH_4 and MgH_2 phases. Thus, the main endothermic peak was the superposition of the Mg_2NiH_4 and MgH_2 dehydrogenation peaks.

The DSC curves of the $Mg_{2-x}Y_xNi_{0.9}Co_{0.1}$ (x = 0.2 and 0.4) alloy hydrides had only one endothermic peak after adding Y. The corresponding peak temperatures for x = 0.2 and 0.4 were 230 and 254 °C, respectively. The XRD analysis of the $Mg_{2-x}Y_xNi_{0.9}Co_{0.1}$ (x = 0.2 and 0.4) alloy hydrides showed that Mg_2NiH_4, MgH_2, YH_3, and $Mg_2NiH_{0.3}$ were the four kinds of decomposable hydrides after hydrogen absorption. Based on DSC curves and XRD analysis, the four hydrides of the desorption processes of the $Mg_{2-x}Y_xNi_{0.9}Co_{0.1}$ (x = 0.2 and 0.4) alloy completely overlapped due to the synergistic effect in the process of hydride desorption.

Comparing the DSC curves of the three alloys, it could be easily determined that the initial dehydrogenation temperature of $Mg_2Ni_{0.9}Co_{0.1}$ alloy was about 200 °C, and the dehydrogenation temperature of Mg_2NiH_4 was 253 °C[33]. This indicates that adding Co could reduce the stability of the alloy hydride, reducing the corresponding hydrogen desorption temperature. The initial desorption temperatures of the $Mg_{1.8}Y_{0.2}Ni_{0.9}Co_{0.1}$ and $Mg_{1.6}Y_{0.4}Ni_{0.9}Co_{0.1}$ alloys were 156 and 208 °C, respectively, indicating that Y was also an effective instability agent, and its addition could reduce the desorption temperatures of the alloys. However, the added Y content affected the improvement degree. The initial hydrogen desorption temperature decreased and then increased with the increased Y content. The improvement was the best when x = 0.2.

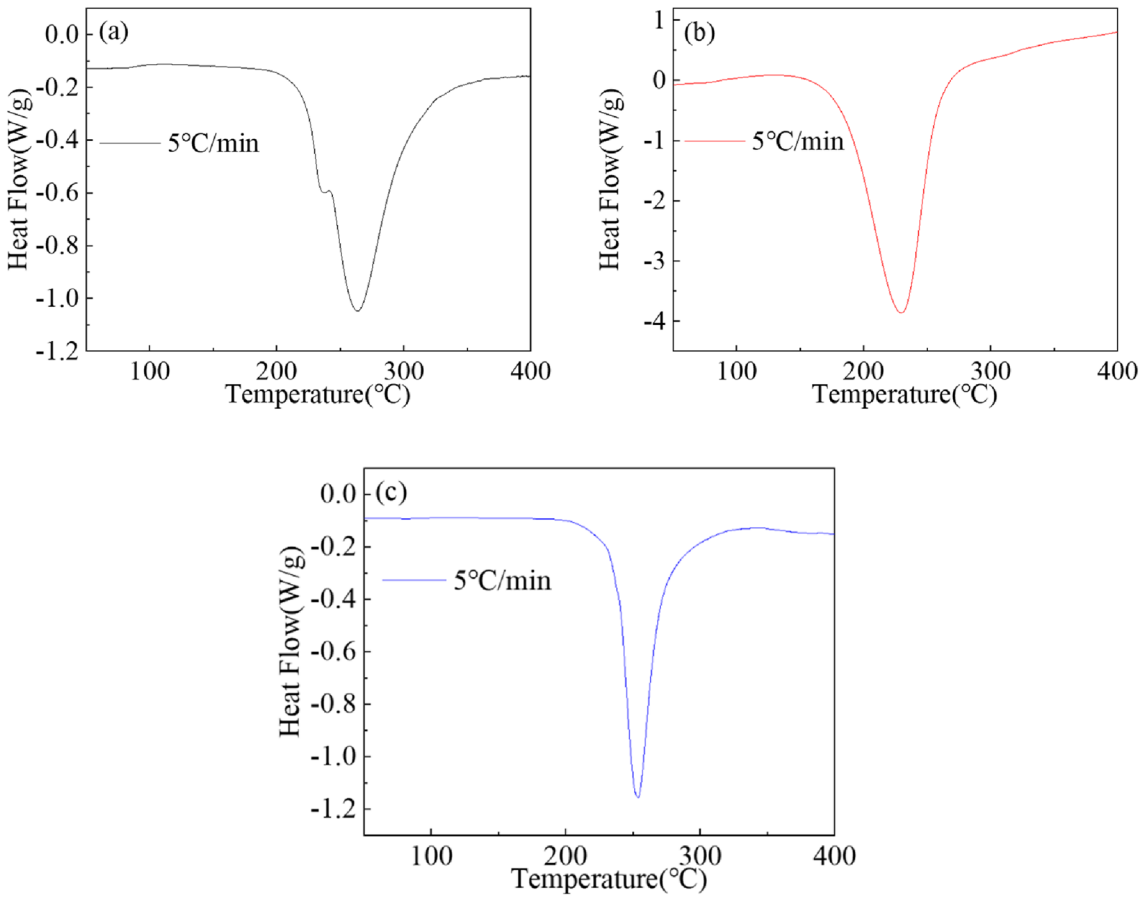

Figure 9. DSC curves of the dehydrogenation of the $Mg_{2-x}Y_xNi_{0.9}Co_{0.1}$ alloy hydrides for (**a**) x = 0, (**b**) x = 0.2, and (**c**) x = 0.4.

The DSC curves of the $Mg_{2-x}Y_xNi_{0.9}Co_{0.1}$ (x = 0 and 0.2) alloy hydrides at different heating rates of 5, 10, and 15 °C/min are shown in Fig. 10. The peak desorption temperatures of the alloys at different heating rates are presented in Table 3. The heating rate affected the peak desorption temperature of the alloy hydrides. The peak desorption temperature increased for both alloys with the increase in the heating rate. The dehydrogenation activation energy E_a is the height of the barrier between the lowest potential energy of the dehydrogenation reactant and the product. The kinetic properties of hydrogen desorption were better for lower activation energies. Furthermore, this study used the peak temperatures of the DSC curves with different heating rates to investigate the dehydrogenation kinetics of the $Mg_{2-x}Y_xNi_{0.9}Co_{0.1}$ (x = 0 and 0.2) alloys. The dehydrogenation activation energy of the $Mg_{2-x}Y_xNi_{0.9}Co_{0.1}$ (x = 0 and 0.2) alloy was calculated according to the Kissinger equation shown in Eq. 8.

$$\ln \frac{\beta}{T_P^2} = A - \frac{E_a}{RT_P} \tag{8}$$

where, β, T_P, E_a, R, and A represent the linear heating rate (°C/min or K/min), the dehydrogenation peak temperature (K), the activation energy for hydrogen desorption (kJ/mol), the gas constant (8.314 J/mol/K), and a linear constant, respectively.

As shown in Fig. 11, the slope of the plot of $\ln(\beta/T_P^2)$ versus $1/T_P$ was E_a/R. Using the slope of the straight line, the calculated dehydrogenation activation energy of the $Mg_2Ni_{0.9}Co_{0.1}$ alloy was 94.7 kJ/mol, slightly lower

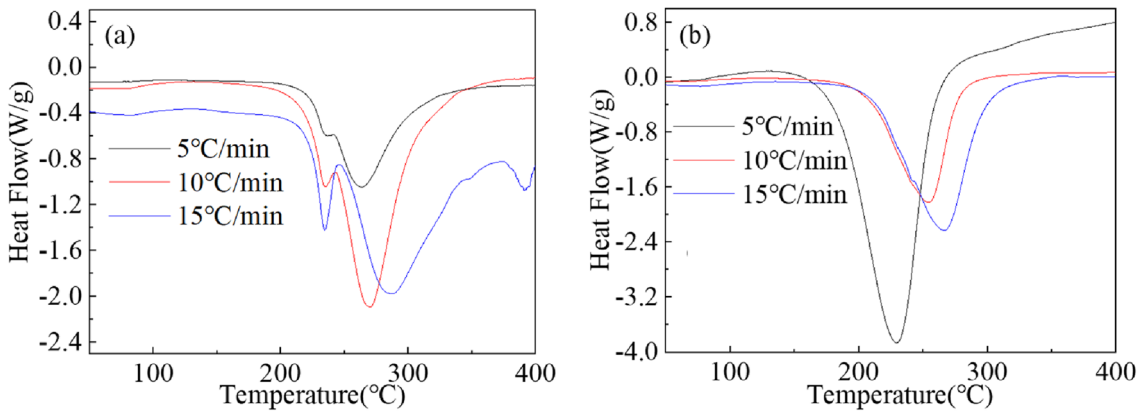

Figure 10. DSC curves of the dehydrogenation of the $Mg_{2-x}Y_xNi_{0.9}Co_{0.1}$ alloy hydrides at different heating rates for (**a**) x = 0 and (**b**) x = 0.2.

Alloy	Peak desorption temperature (°C)		
	5 °C/min	10 °C/min	15 °C/min
x = 0	263	270	288
x = 0.2	230	255	268

Table 3. Dehydrogenation peak temperatures of the $Mg_{2-x}Y_xNi_{0.9}Co_{0.1}$ (x = 0 and 0.2) alloy hydrides at heating rates of 5, 10, and 15 °C/min.

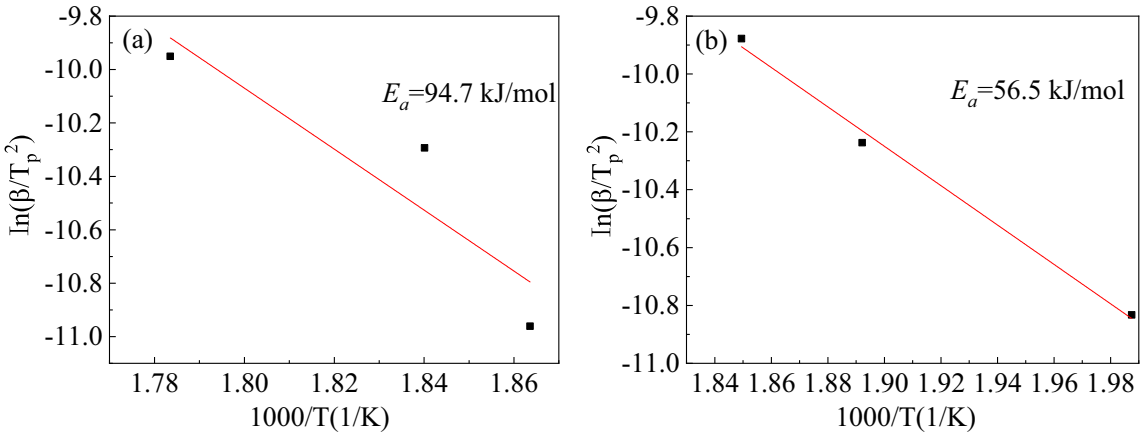

Figure 11. The fitted Kissinger curves of the $Mg_{2-x}Y_xNi_{0.9}Co_{0.1}$ alloy hydrides for (**a**) x = 0 and (**b**) x = 0.2.

than the dehydrogenation activation energy of Mg_2NiH_4 (102 kJ/mol)[34]. The dehydrogenation activation energy of the $Mg_{1.8}Y_{0.2}Ni_{0.9}Co_{0.1}$ alloy was 56.5 kJ/mol, which was much lower than that of the $Mg_2Ni_{0.9}Co_{0.1}$ alloy. The experimental results showed that adding Co and Y could reduce the activation energy of the hydrogen desorption reaction of the Mg_2Ni alloy and improve its hydrogen desorption kinetics. Additionally, the synergistic effect of Co and Y was more obvious than the single addition of Co, which is consistent with the analysis of the hydrogen desorption kinetic curves. The improvement of the dehydrogenation kinetics could be explained from two aspects. The eutectic structure of the alloy was increased and refined with the increase in the added Y content. Several eutectic phase boundaries in the eutectic structure provided an effective way to diffuse hydrogen atoms in the alloy matrix. YH_3 in the hydride could promote the decomposition of MgH_2 in the desorption process, speeding up the desorption reaction rate of the alloys[18].

Conclusions

This study prepared $Mg_{2-x}Y_xNi_{0.9}Co_{0.1}$ (x = 0, 0.2, 0.3, and 0.4) alloys using a metallurgical method to investigate their microstructures and hydrogen storage properties and discuss the effects of the addition of Y on the microstructure and hydrogen storage properties of these alloys. The main conclusions are as follows:

(1) The as-cast $Mg_2Ni_{0.9}Co_{0.1}$ alloy was composed of the peritectic Mg_2Ni, eutectic Mg–Mg_2Ni, and a small amount of the first precipitated Mg–Ni–Co ternary phase. In the absorption process, the Mg_2Ni phase was converted to the Mg_2NiH_4 phase, the Mg_2(Ni, Co) solid solution reacted with hydrogen to form $Mg_2Ni_{0.9}Co_{0.1}H_4$, and the Mg phase was converted to the MgH_2 phase. The Mg–Ni–Co ternary phase was precipitated without hydrogen absorption. After the addition of Y, the $MgYNi_4$ phase and the trace Y_2O_3 phase, along with the Mg and Mg_2Ni phases, were observed in the XRD patterns of the $Mg_{2-x}Y_xNi_{0.9}Co_{0.1}$ (x = 0.2, 0.3, and 0.4) alloys. The phase of the alloy after hydrogen absorption was composed of Mg_2NiH_4, MgH_2, $MgYNi_4$, YH_3, Y_2O_3, and $Mg_2NiH_{0.3}$.
(2) The area ratio of eutectic Mg–Mg_2Ni in the $Mg_{2-x}Y_xNi_{0.9}Co_{0.1}$ (x = 0, 0.2, 0.3, and 0.4) alloys increased, and the eutectic structure was refined with the increased Y content. However, the area ratio of the peritectic Mg_2Ni phase gradually decreased until it disappeared with the increased Y content. In addition to the first precipitated $MgYNi_4$, Y could be dissolved in Mg and Mg_2Ni, increasing the lattice parameters of the corresponding phase.
(3) The test and analysis of the activation properties and de-/hydrogenation kinetics of the alloys showed that the addition of Y improved the activation properties of the alloys. The alloy only needed one cycle to complete the activation when x = 0.4. Although the addition of Y would improve the hydrogen desorption kinetics, it would decrease the hydrogen storage capacity of the alloys.
(4) The addition of Y and Co could decrease the initial dehydrogenation temperature of the Mg_2Ni alloy, and their synergistic effect was more significant than the addition of Co. Combined with hydrogen storage capacity, activation performance, hydrogen desorption temperature, and kinetics, $Mg_{1.8}Y_{0.2}Ni_{0.9}Co_{0.1}$ had the best comprehensive hydrogen storage performance. The maximum hydrogen absorption capacity, the initial desorption temperature, and the dehydrogenation activation energy were 2.07 wt%, 156 °C, and 56.5 kJ/mol, respectively, after complete activation.

Data availability

All data generated or analysed during this study are included in this published article.

Received: 27 September 2023; Accepted: 7 January 2024
Published online: 09 January 2024

References

1. Qi, Y. *et al.* Structure and hydrogen storage performances of La–Mg–Ni–Cu alloys prepared by melt spinning. *Int. J. Hydrog. Energy* **44**(11), 5399–5407 (2019).
2. Yang, T. *et al.* Characterization of microstructure, hydrogen storage kinetics and thermodynamics of a melt-spun $Mg_{86}Y_{10}Ni_4$ alloy. *Int. J. Hydrog. Energy* **44**(13), 6728–6737 (2019).
3. Zhu, Y. *et al.* Hydrogen storage properties of Mg–Ni–Fe composites prepared by hydriding combustion synthesis and mechanical milling. *J. Alloy. Compd.* **520**, 207–212 (2012).
4. Schlapbach, L. & Züttel, A. Hydrogen-storage materials for mobile applications. *Nature* **414**(6861), 1476–4687 (2001).
5. Xu, C. *et al.* Catalytic effect of in situ formed nano-Mg_2Ni and Mg_2Cu on the hydrogen storage properties of Mg-Y hydride composites. *J. Alloys Compd.* **782**, 242–250 (2019).
6. Zhang, Y. *et al.* Microstructure characterization and hydrogen storage properties study of $Mg_2Ni_{0.92}M_{0.08}$ (M = Ti, V, Fe or Si) alloys. *Prog. Nat. Sci. Mater. Int.* **28**(4), 464–469 (2018).
7. Yang, T. *et al.* Evolution of the phase structure and hydrogen storage thermodynamics and kinetics of $Mg_{88}Y_{12}$ binary alloy. *Int. J. Hydrog. Energy* **41**(4), 2689–2699 (2016).
8. Ouyang, L. Z. *et al.* Structure and hydrogen storage properties of Mg_3Pr and $Mg_3PrNi_{0.1}$ alloys. *Scripta Materialia* **61**(4), 339–342 (2009).
9. Luo, S. *et al.* Effect of Al* generated in situ in hydriding on the dehydriding properties of Mg–Al alloys prepared by hydriding combustion synthesis and mechanical milling. *J. Alloys Compd.* **750**, 490–498 (2018).
10. Yang, T. *et al.* Improved hydrogen absorption and desorption kinetics of magnesium-based alloy via addition of yttrium. *J. Power Sources* **378**, 636–645 (2018).
11. Li, J. *et al.* Catalysis and downsizing in Mg-based hydrogen storage materials. *Catalysts* **8**(2), 89 (2018).
12. Xie, L. *et al.* Catalytic effect of Ni nanoparticles on the desorption kinetics of MgH_2 nanoparticles. *J. Alloys Compd.* **482**(1–2), 388–392 (2009).

13. Sun, W. *et al.* The hydrogen storage performance of a $4MgH_2$–$LiAlH_4$–TiH_2 composite system. *J. Alloys Compd.* **676**, 557–564 (2016).
14. Yap, F. A. H. & Ismail, M. The hydrogen storage properties of Mg–Li–Al composite system catalyzed by K_2ZrF_6. *J. Phys. Chem. Solids* **104**, 214–220 (2017).
15. Zheng, J. *et al.* Enhanced reversible hydrogen desorption properties and mechanism of $Mg(BH_4)_2$–AlH_3–LiH composite. *J. Alloys Compd.* **762**, 548–554 (2018).
16. Li, Y. *et al.* Hydrogen storage of casting MgTiNi alloys. *Catal. Today* **318**, 103–106 (2018).
17. Song, W. J. *et al.* Microstructure and hydrogenation kinetics of Mg_2Ni-based alloys with addition of Nd, Zn and Ti. *Trans. Nonferrous Met. Soc. China* **23**(12), 3677–3684 (2013).
18. Kalinicheka, S. *et al.* Structural and hydrogen storage properties of melt-spun Mg–Ni–Y alloys. *Int. J. Hydrog. Energy* **34**(18), 7749–7755 (2009).
19. Li, Y. Z. *et al.* Microstructure characteristics, hydrogen storage kinetic and thermodynamic properties of $Mg_{80-x}Ni_{20}Y_x$ (x = 0–7) alloys. *Int. J. Hydrog. Energy* **44**(14), 7371–7380 (2019).
20. Zhang, T. B. *et al.* Surface valence transformation during thermal activation and hydrogenation thermodynamics of Mg–Ni–Y melt-spun ribbons. *Appl. Surf. Sci.* **371**, 35–43 (2016).
21. Xie, L. *et al.* Synthesis and hydrogen storing properties of nanostructured ternary Mg–Ni–Co compounds. *Int. J. Hydrog. Energy* **32**(12), 1949–1953 (2007).
22. Zhang, H. *et al.* Effect of bimetallic nitride NiCoN on the hydrogen absorption and desorption properties of MgH_2 and the catalytic effect of in situ formed Mg_2Ni and Mg_2Co phases. *J. Alloys Compd.* **965**(25), 171431 (2023).
23. Anik, M., Karanfil, F. & Küçükdeveci, N. Development of the high performance magnesium based hydrogen storage alloy. *Int. J. Hydrog. Energy* **37**(1), 299–308 (2012).
24. Yon, H. *et al.* Dual-tuning of de/hydrogenation kinetic properties of Mg-based hydrogen storage alloy by building a Ni-/Co-multi-platform collaborative system. *Int. J. Hydrog. Energy* **46**(47), 24202–24213 (2021).
25. Yang, H. *et al.* Characteristics of $Mg_2Ni_{0.75}M_{0.25}$ (M = Ti, Cr, Mn, Fe Co, Ni, Cu and Zn) alloys after surface treatment. *J. Alloys Compd.* **330–332**, 640–644 (2002).
26. Song, W. *et al.* Enhanced hydrogen absorption kinetics by introducing fine eutectic and long-period stacking ordered structure in ternary eutectic Mg–Ni–Y alloy. *J. Alloys Compd.* **820**, 153187 (2020).
27. Yartys, V. A. *et al.* Desorption characteristics of rare earth (R) hydrides (R =Y, Ce, Pr, Nd, Sm, Gd and Tb) in relation to the HDDR behaviour of R-Fe-based-compounds. *J. Alloys Compd.* **253–254**, 128–133 (1997).
28. Ding, X. *et al.* Activation mechanism and dehydrogenation behavior in bulk hypo/hyper-eutectic Mg–Ni alloy. *J. Power Sources* **374**(15), 158–165 (2018).
29. Jain, I. P., Lal, C. & Jain, A. Hydrogen storage in Mg: A most promising material. *Int. J. Hydrog. Energy* **35**(10), 5133–5144 (2010).
30. Hayakawa, H. *et al.* Phase transformations among three polymorphs of Mg_2NiH_4. *J. Less Common Met.* **103**(2), 277–283 (1984).
31. Kalinichenka, S. *et al.* Hydrogen desorption kinetics of melt-spun and hydrogenated $Mg_{90}Ni_{10}$ and $Mg_{80}Ni_{10}Y_{10}$ using in situ synchrotron, X-ray diffraction and thermogravimetry. *J. Alloys Compd.* **496**(1–2), 608–613 (2010).
32. Mokbli, S. *et al.* Hydriding and electrochemical properties of amorphous rich Mg_xNi_{100-x} nanomaterial obtained by mechanical alloying starting from Mg_2Ni and $MgNi_2$. *J. Alloys Compd.* **460**(1–2), 432–439 (2008).
33. Song, W. J. *et al.* Microstructure and tailoring hydrogenation performance of Y-doped Mg_2Ni alloys. *J. Power Sources* **245**, 808–815 (2014).
34. Atias-Adrian, I. C. *et al.* Development of nanostructured Mg_2Ni alloys for hydrogen storage applications. *Int. J. Hydrog. Energy* **36**(13), 7897–7901 (2011).

Acknowledgements

Authors gratefully acknowledge the support from [Scientific Research Foundation of Education Department of Anhui Province of China] grant number [2022AH051688], [High-level talents start-up project, West Anhui University] grant number [WGKQ2022016], [Quality engineering project] grant number [006020123153], [Natural Science Foundation of Chongqing, China] grant number [cstc2021jcyj-msxmX0573, cstc2021jcyj-msxmX0743], [Science and technology research program of Chongqing Education Commission of China] grant number [KJQN202201531].

Author contributions

D.L., conception; F.H., L.Z., carrying out measurements; B.R., experimental design; S.W., W.Z., manuscript composition. All authors have read and agreed to the published version of the manuscript.

Competing interests

The authors declare no competing interests.

Additional information

Correspondence and requests for materials should be addressed to F.H.